



# Enhancing Recycling Potential: Exploring Reduction and Metal Separation Behavior of Iron-Rich Slag in Electric Arc Furnace Smelting for a Sustainable Future

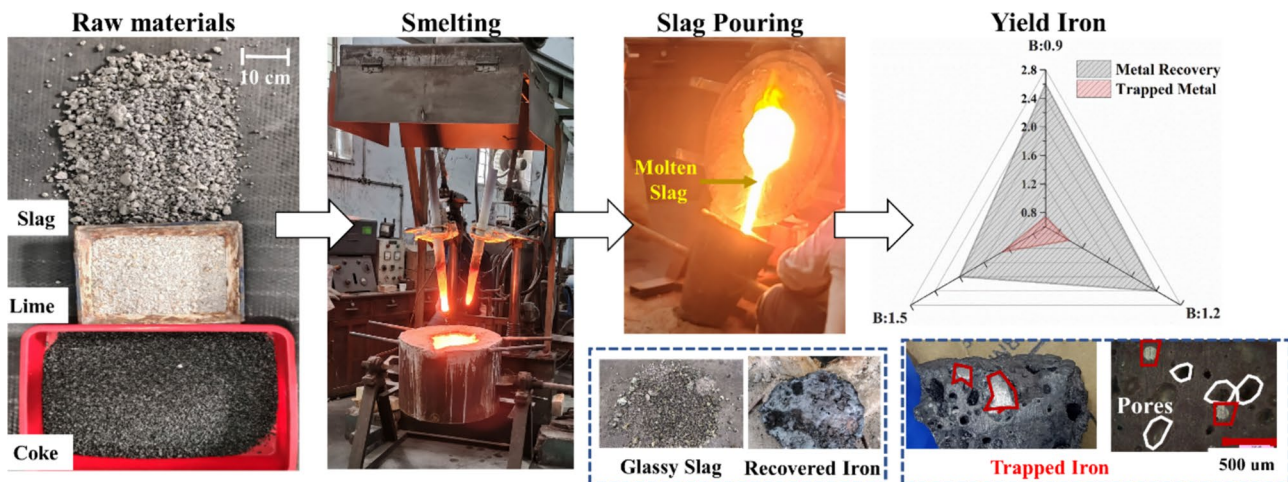
Sheshang Singh Chandel<sup>1,2</sup> · Navneet Singh Randhawa<sup>1</sup> · Prince Kumar Singh<sup>2</sup>

Received: 13 February 2024 / Accepted: 18 June 2024 / Published online: 16 July 2024  
© The Minerals, Metals & Materials Society 2024

## Abstract

The electric arc furnace steelmaking route is essential for sustainable steelmaking through hydrogen-based direct reduced iron. About 30% of the global steel production currently follows the scrap/direct reduced iron–electric arc furnace (DRI-EAF) route, which is bound to increase given decarburization efforts by the steel industry. We investigated DRI-EAF slag recycling simulated in laboratory EAF smelting tests to lower its environmental impact. Several aspects of process development were explored, such as process conditions, specific energy consumption, and the settling behavior of iron particles. Significant reductions occur in the first 15 min, ranging from 73.4% to 83.34%. About 97% iron was recovered under optimum conditions: basicity—1.2, carbon/oxygen ratio—1, and time—40 min. The settling velocities of iron particles decreased with increasing slag basicity, reaching values of  $3.13 \times 10^{-5}$  m/s,  $1.95 \times 10^{-5}$  m/s, and  $0.89 \times 10^{-5}$  m/s for basicities 0.9, 1.2, and 1.5, respectively. The effects of basicity on slag viscosity, phase formation, and energy consumption are critically discussed. Compared to 0.9, basicities of 1.2 and 1.5 increase power consumption by 17.6% and 23.5%, respectively. The findings potentially contribute to managing DRI-EAF-based slag, repositioning it as a potential resource, and reducing associated pollution.

## Graphical Abstract



**Keywords** Electric arc furnace · Iron · Recycling · Settling behavior · Steel Slag

The contributing editor for this article was Yongxiang Yang.

Extended author information available on the last page of the article

## Introduction

Steel slag is a byproduct generated during the smelting of iron ores and fluxes. About 30% of the world's steel is produced by the electric arc furnace (EAF) route. As per the World Steel Organization, the worldwide production of steel slag in 2019 amounted to approximately 432 million metric tons (MT), with India contributing 32 million metric tons (MT) to this total. [1]. A statistical analysis determined that the electric arc furnace method alone generated 7 million metric tons (MT) of slag in India annually in 2018 [2]. This figure subsequently increased to 9 million MT in 2019 and 18 million MT in 2022. The significant issue faced by the metallurgical sector is the high volume of slag formation. In contrast to blast furnace slag, steel slag lacks a distinct recycling pathway. Consequently, most of this slag is in landfills, causing substantial covering of usable land and leading to health-related issues. The potentially high pH level of EAF slag dust has been linked to irritation of the skin and respiratory system when inhaled or touched for extended periods (USEPA, 2023). EAF slag may also contain hexavalent chromium and manganese. Hexavalent chromium can cause cancer, and an excess of manganese in the body can harm the nervous system. Children's physiology and behavior differ from adults, making them more susceptible to toxins. Hence, a sustainable operation of steel production by EAF warrants potential slag recycling in the circular economy.

The EAF slag is abundant in minerals such as iron, calcium, silica, aluminum, and numerous others. This composition signifies the recycling and reutilization of slag in various metallurgical industrial applications and other industries. EAF slag has been explored for various applications, including road-building aggregates, cementitious material, ceramics, etc. [3]. However, tangible recycling has not resulted due to the metallic iron content in the slag. The total iron content of EAF slag generally ranges from 20 to 35% [4]. However, the metallic iron embedded in the slag phase is not fully recoverable physically [5]. The most abundant iron phases are FeO, Fe<sub>2</sub>O<sub>3</sub>, and Fe<sub>2</sub>SiO<sub>4</sub>. Lately, several investigations have encompassed approaches to extracting iron content from slag, including mechanical metallurgy, hydrometallurgy, and pyrometallurgy. Among all the routes considered, it was determined that pyrometallurgical via carbothermic reduction is one of the most suitable methods for extracting iron from various complex material structures. Some small-scale studies demonstrate the possibilities of iron extraction from EAF slag in the presence of reducing agents and fluxes. There are two reducing agents: (a) solid carbon in the form of coke, charcoal, graphite, etc., and (b) gases like hydrogen, carbon monoxide, and natural gases. The reduction of EAF

slag is a multiphase reaction either by direct reduction in the presence of solid carbon or through indirect reduction when a gas acts as a reductant. A direct and indirect reduction occurs combined as the slag undergoes gradual heating up to a melt phase. Nevertheless, the available data are scarce to adopt the carbothermic reduction of EAF slag for upscale, particularly for a large setup.

In this investigation, a smelting reduction of EAF Slag was carried out in an AC electric arc furnace to determine the critical parameters for effective reduction strategy and, eventually, the parameters optimization. Metallurgical coke and fluxes are utilized to maintain the favorable reduction behavior. Thermodynamic and smelting kinetics were thoroughly analyzed to investigate the smelting behavior of the slag. The results from EAF smelting tests were determined to be helpful in yield, recovery, and specific power consumption. The formation of iron particles in the molten slag, the growth of iron, and the settling behavior of iron particles were discussed. A plausible mechanism for the carbothermic reduction of the EAF slag was proposed. The present studies will contribute to sustainable steel production operations via the EAF route.

## Material and Methods

### Raw Materials

Electric arc furnace slag (EAFS) was sourced from the Indian steel industry and generated as a byproduct of a mild steel scrap melting process of a 15 MVA EAF. About 100 kg of raw slag were homogenized and utilized in the present study. The EAFS had a porous structure, a blackish hue, and a lumpy appearance, which was crushed into < 250 mm using an industrial crusher for optimal handling in smelting tests, as shown in Fig. 1a. The coning and quartering technique for characterization obtained a representative sample.

The other raw materials, namely, coke and lime (CaO), were of commercial grade, and their chemical composition is given in Table 1. The smelting experiment used the size range of 2–2.83 mm and 4–4.76 mm for coke and lime, respectively. Mesh numbers 7 and 10 were used to obtain the mentioned size fraction of coke, and mesh numbers 4 and 5 were used to obtain the lime particles.

### Characterization Methods

The chemical composition of EAFS was determined by combining ASTM wet chemical and instrumental methods [6]. The phase analysis of samples was carried out with the help of the Bruker D800 X-ray diffractometer. The CuK $\alpha$  radiation was used to measure the diffractogram of sample 10° to 80° 2 $\theta$  range with a scanning rate of 2°/sec. Figure 1b

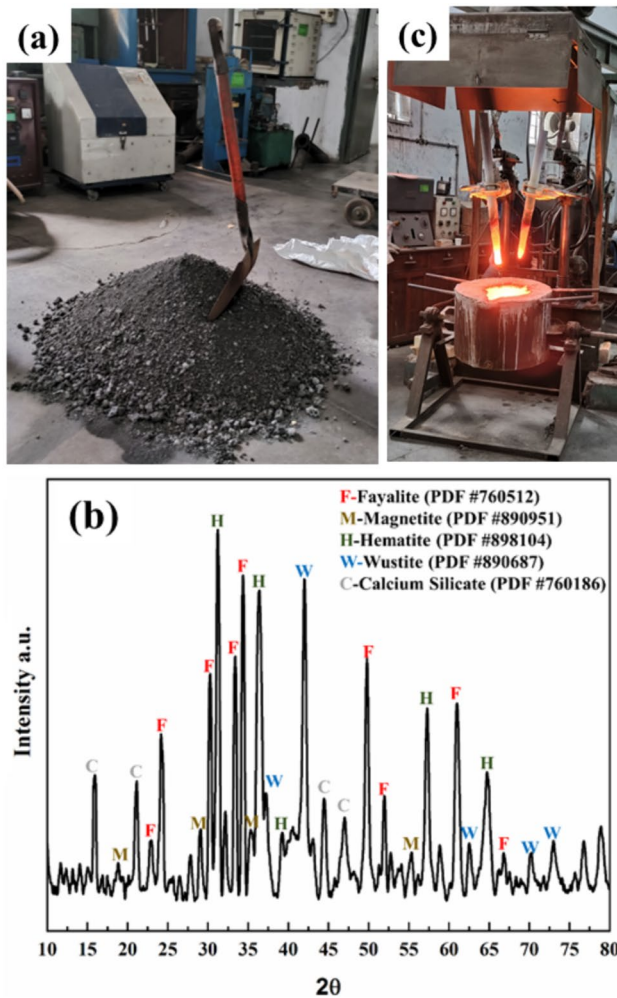


**Fig. 1** a 100 kg of EAF slag, b XRD spectrogram of EAF slag, and c Two-phase electric arc furnace

shows the XRD analysis of EAF slag. The primary phases identified by XRD analysis are fayalite ( $2\text{FeO}\cdot\text{SiO}_2$ ), hematite ( $\text{Fe}_2\text{O}_3$ ), wustite ( $\text{FeO}$ ), with minor amounts of magnetite ( $\text{Fe}_3\text{O}_4$ ) and calcium silicate ( $2\text{CaO}\cdot\text{SiO}_2$ ). The physical detection and elemental distribution were done with the help

of SEM–EDS (JEOL-6610LV). The multiple-point analysis carried out determined the elemental associations and predictable phases. The optical microscope (Leica Microsystems) detected the trapped iron in slag in a cross-section sample prepared by cutting and polishing [7]. The calculation of the density of furnace slag and reduced metal was done with the help of Archimedes' principle in analytical weighing balance (METTLER TOLEDO XPR226DRQ) at room temperature, and slag viscosity was calculated with the help of FactSage® 8.0 software using FactPS, FToxid, and FTmisc database for resulting slag compositions.

## Smelting Furnace

Reduction smelting experiments were carried out in a two-phase electric arc furnace of 10 kg capacity, as shown in Fig. 1c. The furnace consists of two graphite electrodes (50 mm dia.), a furnace shell with a working line of MgO mass. Each graphite electrode was fitted into a water-cooled copper clamp and connected to a phase point of the 50 kVA AC power source. The electrode-holding clamp was connected to mechanically movable arms, which can be moved vertically and horizontally with a handle on a column for positioning the electrode. The furnace was covered with a lid made of refractory-lined two halves with the provision at the middle for electrode entry.

## Smelting Procedure

The < 50 mm-sized EAF slag was utilized in the smelting. The charge material was prepared based on stoichiometric calculations of coke and slag for several carbon/oxygen (C/O) ratios of 0.5 to 1.5. The basicity ( $B = \text{CaO}/\text{SiO}_2$ ) of slag was maintained for 0.9, 1.2, and 1.5 by adjusting lime and quartz in the charge mix. The furnace was preheated to approximately 1200 °C for each experiment by arcing on coke.

A typical smelting experiment was divided into (a) the charging and melting of material and (b) the smelting or reaction stage (Fig. 2). Raw materials were charged and

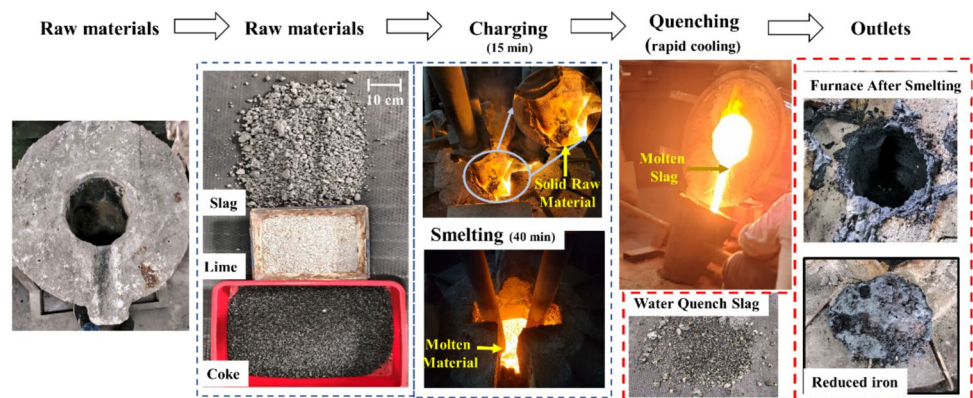
**Table 1** Chemical analysis composition of industrial EAF slag materials, coke, and lime

Wt. %	Total Fe	FeO	Metallic Fe	CaO	SiO <sub>2</sub>	Al <sub>2</sub> O <sub>3</sub>	MgO	MnO	S	P
EAFS	35.5	25.18	2.7	20.68	17.21	18.21	8.18	4.73	0.16	0.15
Constituent	FC	VM	Ash	Moisture	Fe <sub>2</sub> O <sub>3</sub>	CaO	SiO <sub>2</sub>	Al <sub>2</sub> O <sub>3</sub>	MgO	
Proximate analysis					Chemical composition					
Coke (Wt%)	74.02	1.83	22.96	1.16	3.77	1.09	32.77	61.90	0.46	
Lime (Wt%)	–	–	–	–	0.11	92.01	1.51	0.96	6.15	

FC Fixed Carbon

VM Volatiles matter, LOI of lime: 8.9 Wt%

**Fig. 2** Experimental procedure for iron recovery from electric arc furnace slag



melted within 15 min for all the experiments. After melting the raw material into the furnace, the smelting or reaction is allowed for 40 min. The iron reduction behavior during the smelting process was monitored by collecting the samples every 5 min with the help of a 5-mm-diameter iron bar and quenching in water. In the end, the slag was quenched in water for rapid cooling, while some slag was left in the furnace for slow cooling. The cooled slag was ground to 100 mesh BSS powder and analyzed for phases and chemical composition of secondary slag.

## Results and Discussion

### Thermodynamic of EAF Slag Reduction

In a carbothermic reduction process, iron oxides undergo reduction by carbon in basically two modes of reactions. [8, 9]. In the direct reduction, the solid carbon reacts with iron oxides, which get oxides and form CO gas, as shown by Eqs. 1, 2, 6, and 8. However, the indirect reduction is essentially carried out by the CO gas, which reduces the iron oxide forming CO<sub>2</sub> gas and Fe, as shown by Eqs. 3, 4, 7, and 9. The temperature at  $\Delta G=0$ , Gibbs free energy ( $\Delta G$ ), and enthalpy ( $\Delta H$ ) value at 300 K were calculated

using FactSage® 8.0 for Eqs. (1–9), and are given in Table 2. Most reactions (Eqs. 1–8) occur below 1100 K, i.e., in the solid state. Interestingly, reducing fayalite by CO is not feasible in normal operating conditions like 1673–1873 K when CaO is present. The  $\Delta G$  for all reactions was calculated with the help of FactSage® 8.0 [10], shown in Fig. 3. Figure 3a shows the calculation of  $\Delta G$  for the direct and indirect reduction of hematite and wustite, which follows Eqs. (1–4). The equations represent the effect of CaO on the  $\Delta G$  (8–9), as shown in Fig. 3b. The free energy change ( $\Delta G$ ) concerning the temperature graph shows that the higher the negative value of  $\Delta G$ , the more spontaneous the reaction occurs at a specific temperature. As per Fig. 3a and b, reducing iron oxides from slag using direct reduction was preferable above 830 K; below that, CO gas performs better for the reduction. Nevertheless, the effect of indirect reduction using CO gas was very low at 1873 K, as reported earlier. [11, 12].

### Reduction Behavior of EAFS

Each smelting experiment reduced 10 kg of EAF slag using different stoichiometric carbon contents. The experiment proceeded through three stages, as depicted in Fig. 4a–c. The charging was completed within 15 min. After that, slag samples were periodically withdrawn to

**Table 2** Chemical reactions for the reduction of slag by carbon

Equations	$T_{\Delta G=0}$ K	$\Delta G_{300K}$ KJ	$\Delta H_{300K}$ KJ	Eq. no
$\text{Fe}_2\text{O}_3 + \text{C} \rightarrow 2\text{FeO} + \text{CO}(\text{g})$	831	116.67	183.62	(1)
$\text{FeO} + \text{C} \rightarrow \text{Fe} + \text{CO}(\text{g})$	998	107.42	155.29	(2)
$\text{FeO} + \text{CO}(\text{g}) \rightarrow \text{Fe} + \text{CO}_2(\text{g})$	901	-123.7	-171.9	(3)
$\text{Fe}_2\text{O}_3 + \text{CO}(\text{g}) \rightarrow 2\text{FeO} + \text{CO}_2(\text{g})$	119	-312.6	111.30	(4)
$\text{C} + \text{CO}_2(\text{g}) \rightarrow 2\text{CO}(\text{g})$	981	119.80	172.49	(5)
$2\text{FeO} \cdot \text{SiO}_2 + 2\text{C} \rightarrow 2\text{Fe} + 2\text{CO}(\text{g}) + \text{SiO}_2$	1068	250.00	348.81	(6)
$2\text{FeO} \cdot \text{SiO}_2 + 2\text{CO}(\text{g}) \rightarrow 2\text{Fe} + 2\text{CO}_2(\text{g}) + \text{SiO}_2$	558	10.403	3.8320	(7)
$2\text{FeO} \cdot \text{SiO}_2 + 2\text{C} + \text{CaO} \rightarrow 2\text{Fe} + 2\text{CO}(\text{g}) + \text{CaO} \cdot \text{SiO}_2$	511	71.936	85.519	(8)
$2\text{FeO} \cdot \text{SiO}_2 + 2\text{CO}(\text{g}) + \text{CaO} \rightarrow 2\text{Fe} + 2\text{CO}_2(\text{g}) + \text{CaO} \cdot \text{SiO}_2$	<2500	-167.0	-83.67	(9)

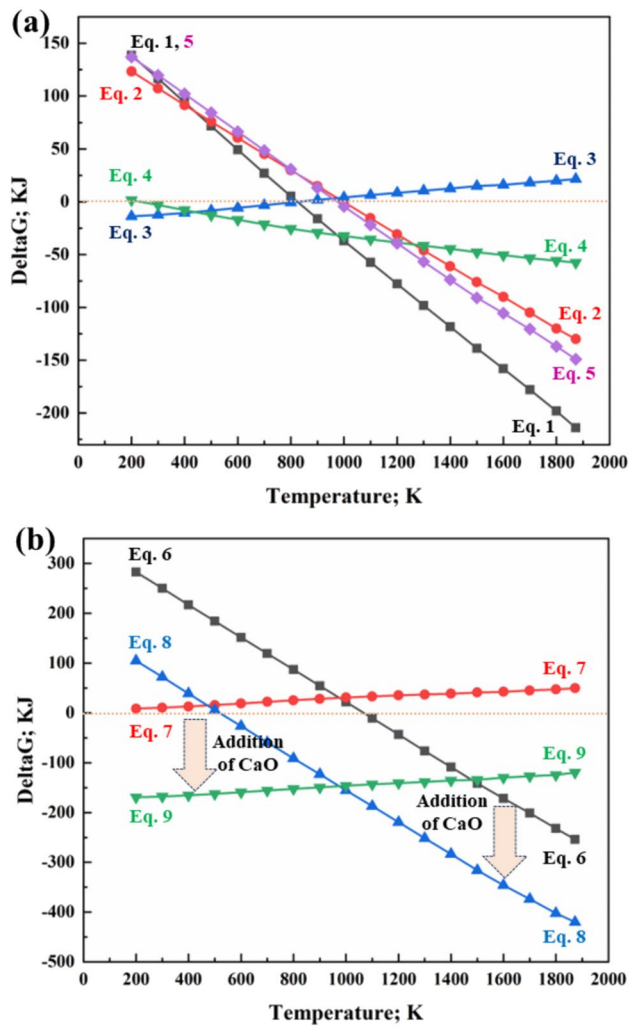


**Fig. 3** Change of Gibbs free energy concerning temperature for **a** Eqs. 1–5 and **b** Eqs. 6–9

study the reduction process by analyzing their FeO content. Figure 5a shows the withdrawal of the sample by using a steel rod. Quenching and collection of the sample are schematically shown in Fig. 5b. Eight samples from each test were collected to study the reduction behavior of iron during 40 min of the experiment. Each of the samples was analyzed in triplicate to determine the FeO content. Figure 5c shows the color contrast collected from black to brown to white–gray. The gradual color change can be attributed to the decreasing iron content of the slag. Higher iron content in slag has a blackish appearance; the lighter color represents the lower iron content, and white slag shows a total iron content of less than 2%. The slag samples were not homogenous, so each was ground and mixed thoroughly. The homogeneous samples were analyzed in triplicates, and average values are depicted in Fig. 6a and b.

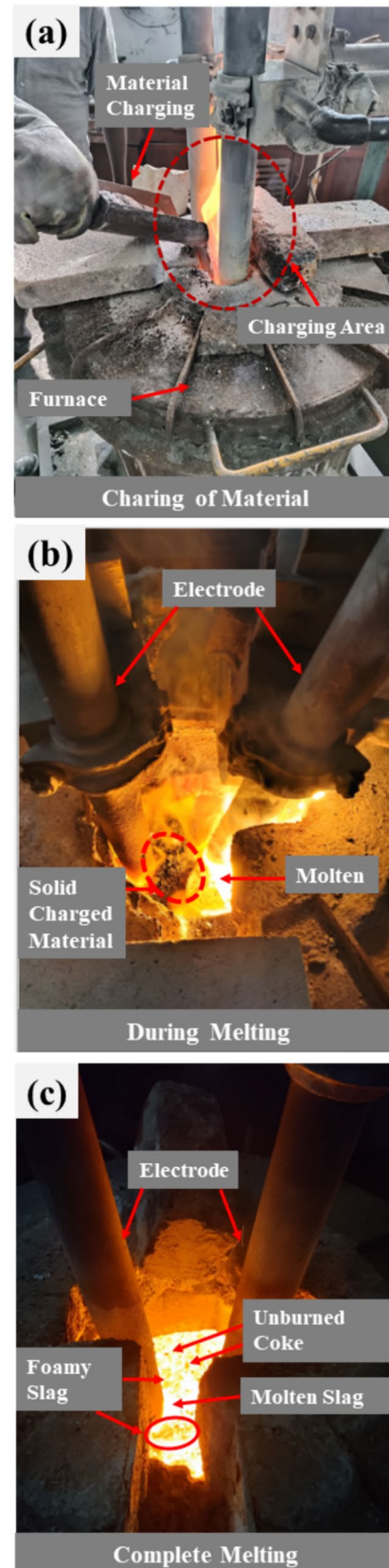


**Fig. 4** Reduction steps **a** charging of material in the furnace, **b** melting of charge material, and **c** complete melting and chemical interaction

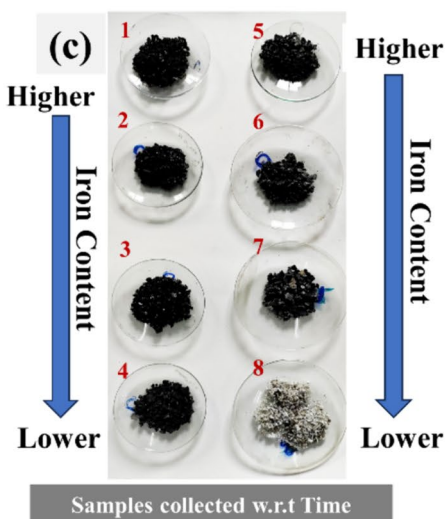
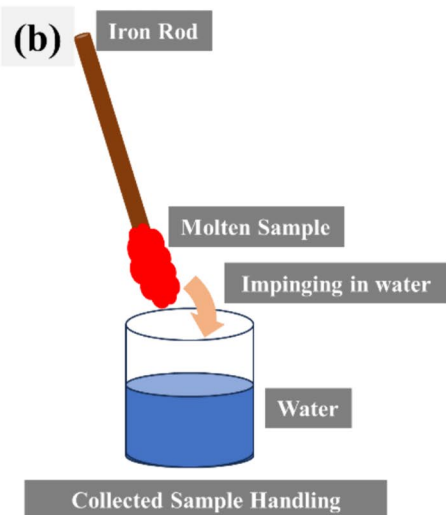
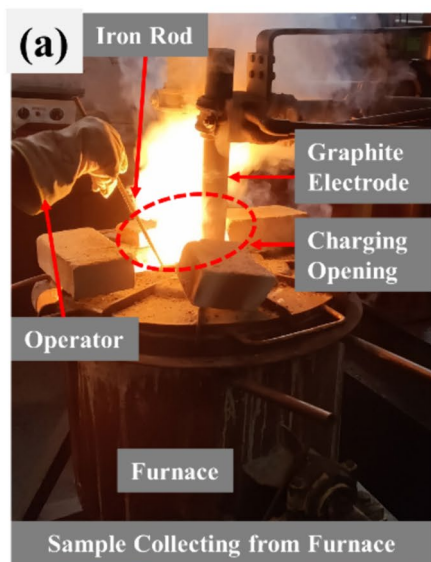


Fig. 5 Collecting steps of slag sample during the experiment: **a** sample collection from the furnace, **b** handling of molten slag sample, and **c** over time sample collection

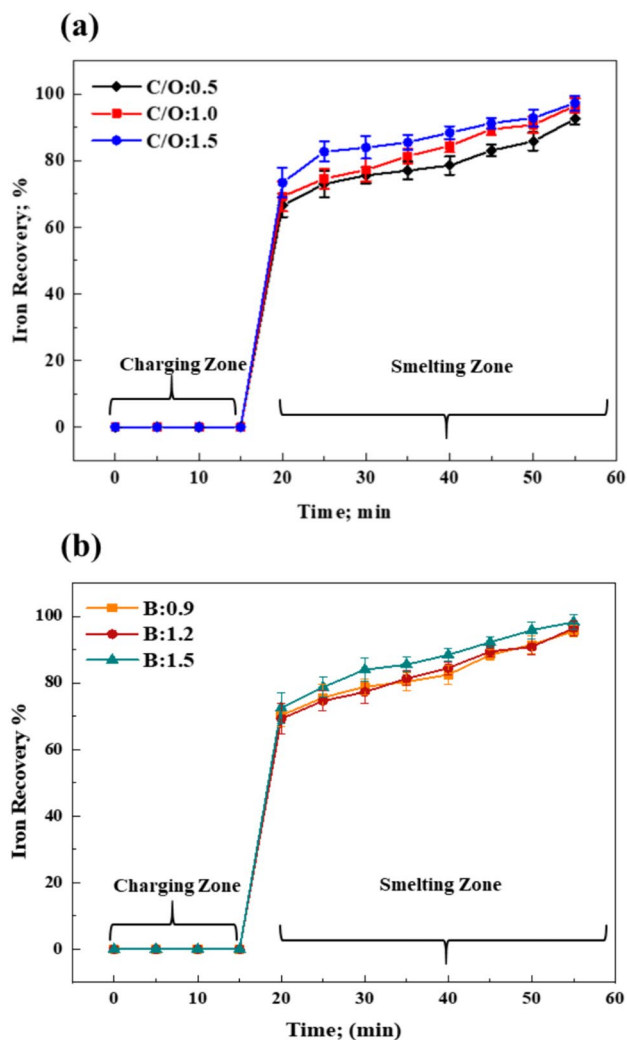


Fig. 6 Reduction of iron from EAFs **a** when the C/O ratio varies with a fixed B = 1.2 and **b** when B is varied with a fixed C/O of 1.0

**Effect of Carbon/Oxygen Ratio**

The addition of carbon controlled by varying the Carbon/Oxygen (C/O) stoichiometric ratios significantly affects the reduction process. Figure 6a shows the reduction behavior as the degree of reduction ( $\alpha$ ) of total iron with different C/O ratios in slag over time. The initial reduction of total iron in the first 15 min of slag smelting is  $73 \pm 4\%$ ,  $75 \pm 2.8\%$ , and  $83 \pm 3.4\%$  for C/O 0.5, 1.0, and 1.5. The apparent reduction rate is relatively fast for the first 15 min when melting and smelting go simultaneously, which signifies the direct reduction of the solid charge. After melting, the indirect reduction progresses steadily in the liquid phase and becomes constant after 40 min. The final reduction of iron at the end of the smelting experiment with the C/O ratio 0.5, 1.0, and 1.5 are  $92.3 \pm 2.1\%$ ,  $97.2 \pm 2.5\%$ , and  $97.8 \pm 2.2\%$ . A stoichiometric addition of carbon is helpful to obtain a nearly complete

reduction of iron from EAFs. However, it is notable that a higher stoichiometric ratio than unity (i.e., 1.5) leaves unreacted coke at the end of the experiment, as shown in Fig. 4c.

### Effect of Flux

Adding lime (CaO) as a flux improves the reduction of iron in the EAF slag. Increasing the slag basicity above 1.2 enhances the degree of iron reduction, while decreasing below 1.2 diminishes the reduction. For instance, the initial reduction of total iron in the first 15 min of slag smelting is  $75.4 \pm 1.9\%$ ,  $75 \pm 2.8\%$ , and  $79.1 \pm 3.8\%$  for B 1.0, 1.2, and 1.5. Slag basicity 1.5 shows the highest overall degree of reduction at 98.3% by the end. The improved reduction with basicity 1.5 is attributed to the favorable reactions between CaO and  $\text{Fe}_2\text{SiO}_4$ . Adding lime provides additional  $\text{Ca}^{2+}$  ions that interact with fayalite, forming  $\text{CaSiO}_3$  and  $\text{Fe}_2\text{O}_3/\text{Fe}_3\text{O}_4$  (Eqs. 9, 10, 11). The thermodynamic activity of FeO is enhanced by lime addition, further promoting iron reduction [13]. The effect of slag basicity is crucial for slag–metal separation behavior. Slag basicity governs various physico-chemical properties of the CaO–SiO<sub>2</sub>–Al<sub>2</sub>O<sub>3</sub> slag system, and the viscosity is considered essential for the metal–slag separation behavior. Tables 3 and 4 show the chemical composition of recovered iron and water-quenched slag.

### Mineralogy of Modified Slag

The mineralogical composition of a slag is critical for its potential in various applications. Rapid cooling of blast furnace slag produces a glassy phase suitable for cement production [14]. Water quenching is currently the most effective method for obtaining glassy slag [15]. The slag obtained in each experiment was rapidly and slowly cooled

in this study for mineralogical comparison. Slow-cooled slag exhibited high-intensity peaks due to higher crystallinity than rapid-cooled slag. The peaks indicated the presence of Akermanite ( $\text{Ca}_2\text{Mg}(\text{Si}_2\text{O}_7)$ ), Gehlenite ( $\text{Ca}_2(\text{Al}, \text{Mg})(\text{Si}, \text{Al})\text{SiO}_7$ ), calcium aluminum oxide ( $\text{Al}_{14}\text{Ca}_{12}\text{O}_{33}$ ), dicalcium silicate ( $\text{Ca}_2\text{SiO}_4$ ), and iron oxides, shown in Fig. 7a–b. Water-quenched slag had a lower peak intensity, indicating a glassy phase. It consisted of phases usually found in granulated blast furnace slag [15]. The primary phases consisted of dicalcium silicate and calcium aluminum oxide. The slow-cooled and rapid-cooled slags contained metallic iron, indicating iron entrapment in the slag phase. However, the rapid-cooled slag generated finer slag particles separating the entrapped iron particles, generating a cleaner slag.

On the other hand, the slow-cooled slag was contaminated with entrapped iron particles. The photographic and microscopic images of slow-cooled slag in Fig. 8a–d illustrate the presence of iron particles in the slag. The cross-sectional image of the slag reveals a substantial amount of porous structure on the surface of the slag, as well as a wide range of iron particle sizes. The cross-sectional appearance of the slag led to the conclusion that iron agglomeration and growth occurred during slow cooling, resulting in a wide range of iron particle sizes. As shown in 9(d), a microscopic image of a slag cross-section reveals that the trapped iron particles are nearly spherical.

### Optimum Reduction Conditions

Figure 9 shows the yield and trapped metal content for different kilograms of slag basicities. The maximum yield was observed with the basicity 0.9, which is 70.4%, which follows a decreasing trend with the increasing slag basicity. For instance, the yield is 56.33% for basicity 1.5. In

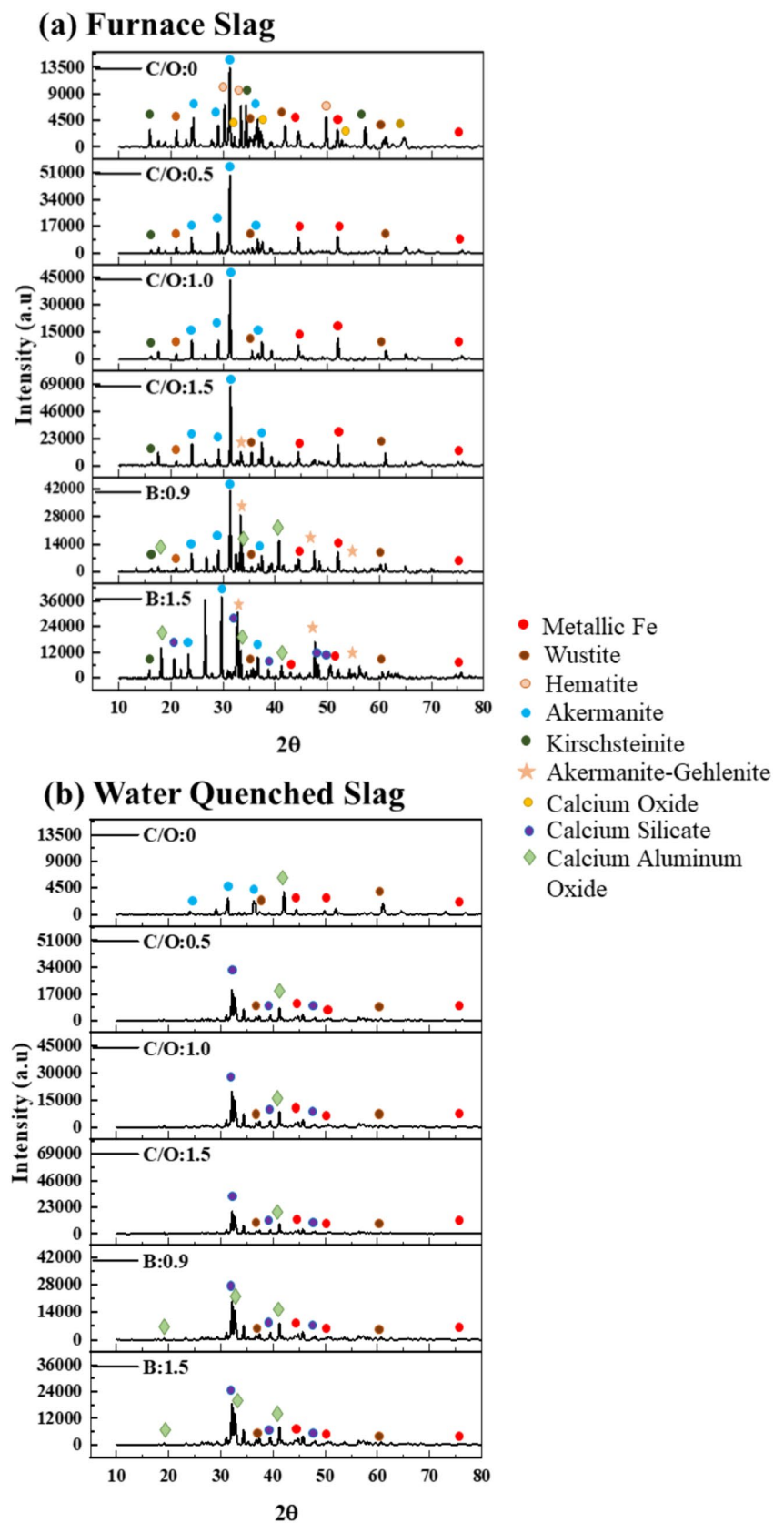
**Table 3** Chemical composition of the extracted metal

Sample	Fe, %	Al, %	Si, %	S, %	P, %	C, %	Cr, %	Mg, %	Mn, %	Mo, %
EAF-CO0.5	89.2	0.04	0.09	0.125	0.20	3.87	0.69	0.05	0.16	0.009
EAF-CO1.0	88.5	0.05	1.88	0.021	0.48	4.47	3.12	0.03	4.37	0.017
EAF-CO1.5	91.2	0.85	1.38	0.17	0.55	4.56	1.23	0.4	1.81	0.007
EAF-B0.9	90.4	0.00	0.81	0.019	1.17	4.15	2.75	0.05	3.27	0.016
EAF-B1.5	90.7	0.17	4.91	0.024	0.81	3.17	1.44	0.05	3.62	0.007

**Table 4** Chemical composition of slag

Sample	Total Fe %	FeO %	Fe (M) %	CaO %	SiO <sub>2</sub> %	Al <sub>2</sub> O <sub>3</sub> %	MgO %	S %	P %	TiO <sub>2</sub> %	Cr <sub>2</sub> O <sub>3</sub> %
EAF-CO0.5	2.22	2.36	0.09	34.0	28.5	17.57	9.7	0.19	0.16	0.78	0.73
EAF-CO1.0	1.50	0.97	1.88	36.1	29.2	17.00	8.2	0.56	0.04	0.25	0.07
EAF-CO1.5	2.22	3.18	1.38	35.8	27.3	18.57	8.5	0.20	0.17	0.77	0.77
EAF-B0.9	3.56	2.10	0.81	37.0	26.0	13.26	7.2	0.71	0.07	0.32	0.12
EAF-B1.5	1.31	0.2	4.91	53.4	43.7	12.98	7.4	0.42	0.03	0.15	0.03

**Fig. 7** XRD analysis of **a** Furnace slag (slow cooling) and **b** Water-quenched slag (rapid cooling)





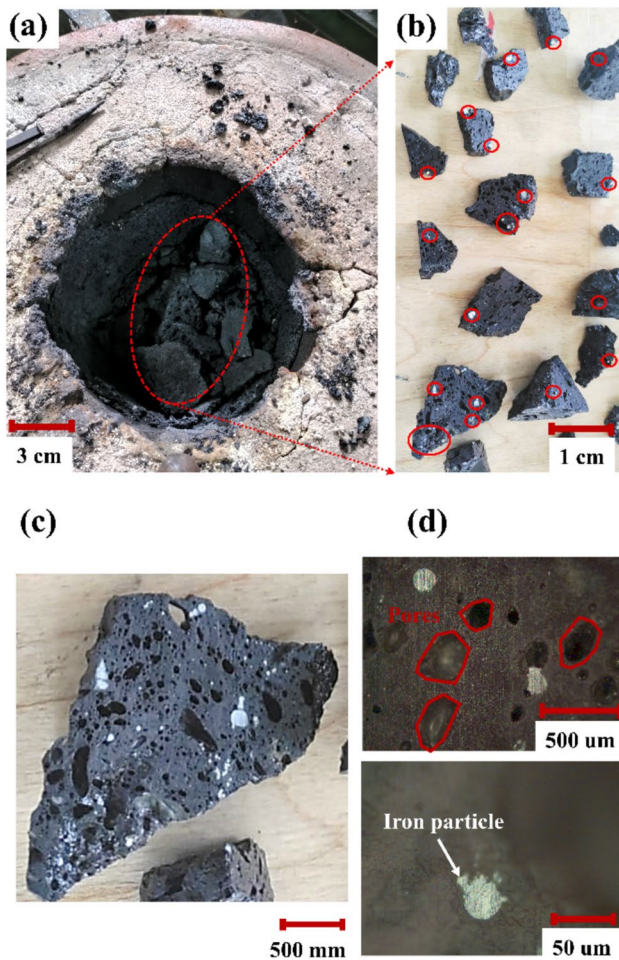
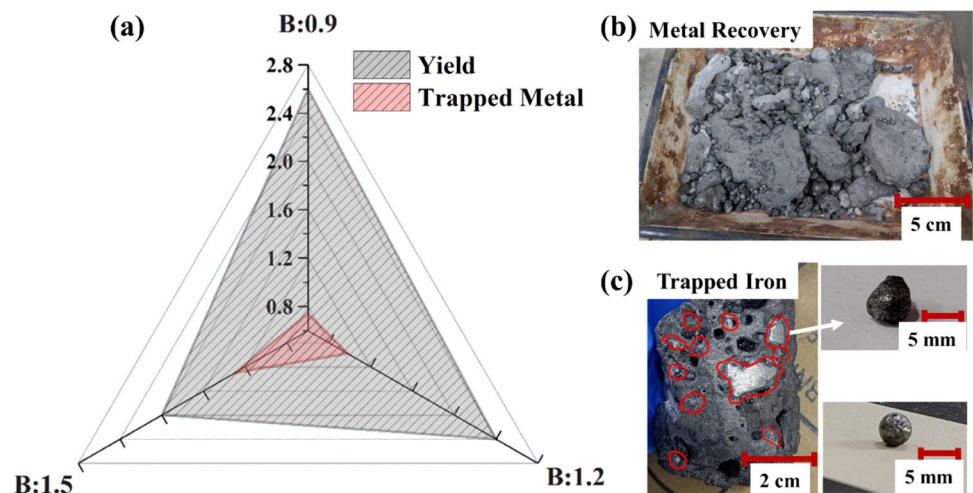


**Fig. 8** **a** Slow-cooled slag inside furnace, **b** cross section, **c** magnified cross section, and **d** Microscopic image of the slow-cooled slag

contrast, the entrapment of metal particles in slag increases with slag basicity, which is 25.3%, and increases to 28.1% for basicity 1.5. Such entrapment of metal particles can be

**Fig. 9** **a** The Yield in Kg for various slag basicity experiments, **b** Visual evidence of settling iron, and **c** trapped iron during the recovery process



attributed to slag fluidity, which increases when basicity increases from 0.9 to 1.5. The slag fluidity tends to increase when the basicity is beyond unity because of solid phases at 1873 K. The addition of calcium during the smelting process replaced iron, which is associated with silica and aluminum, and developed calcium-based phases, as shown in the XRD data. Those phases, e.g.,  $\text{CaSiO}_3$ ,  $2\text{CaO}\cdot\text{SiO}_2$ , and  $\text{CaO}\cdot\text{SiO}_2$ .  $\text{Al}_2\text{O}_3$  have higher melting temperature than the process temperature, causing a decrease in the slag fluidity [16]. The precipitation of such phases causes a decrease in slag fluidity value, which restricts settling the iron particles trapped in the slag layer. Moreover, some amount of unrecovered iron was also found. In low basicity slag, the unrecovered iron particles are around 4.3%, whereas, for higher slag basicity, it increases to 15.57%. This observation also denotes higher micro-sized iron particles in higher than lower basicity.

### Settling Behavior of Iron Particles

During the reduction smelting of slag in EAF, the density difference between molten metal particles and molten slag causes natural separation at smelting temperature. Slow slag cooling allows iron particles to settle to the bottom, resulting in large particle sizes with irregular spherical shapes. ImageJ software calculates mean diameters of 65  $\mu\text{m}$ , 52  $\mu\text{m}$ , and 38  $\mu\text{m}$  for 200 iron particles (Fig. 10). Significant diameter variation was observed for slag basicity 1.2 compared to 0.9 and 1.5. The terminal velocity of molten metal particles during settling was studied using Stoke equations (Eq. 10), considering density and viscosity values for different slag compositions.

$$V_1 = \frac{gd^2(\rho_m - \rho_s)}{18\mu_s} \quad (10)$$

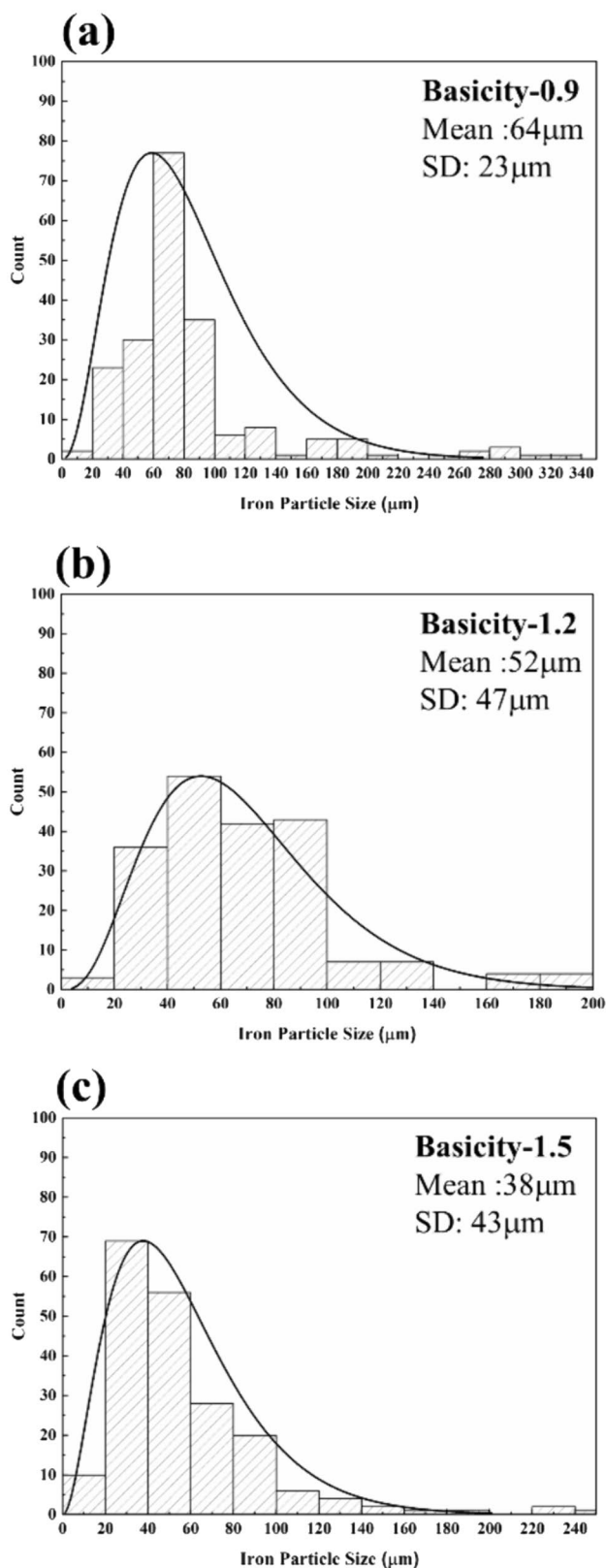


Fig. 10 Mean particle size of trapped iron and its standard variation

Here,  $V_1$  is the terminal velocity of the iron particle during settling;  $g$  is the acceleration due to gravity  $9.81 \text{ m/s}^2$ ;  $d$  is the diameter of the iron particle ( $m$ );  $\rho_M$  is the density of iron particle  $4835 \text{ kg/m}^3$  [17];  $\rho_s$  is the density of EAF slag for basicities 0.9, 1.2, and 1.5, which are  $3634 \text{ kg/m}^3$ ,  $3447 \text{ kg/m}^3$ , and  $3215 \text{ kg/m}^3$  and viscosity ( $\mu_{slag}$ ) of EAF slag in Pa.s. The  $V_i$  calculated for the molten metal particles are  $7.31 \times 10^{-6} \text{ m/s}$ ,  $4.14 \times 10^{-6} \text{ m/s}$ , and  $1.67 \times 10^{-6} \text{ m/s}$ . The calculated terminal velocities corresponded to travel times of 1402 s, 2415 s, and 5988 s to travel one centimeter in height.

Slag cooling was also an important factor affecting the settling velocity and the deformation of iron particles due to drag [17]. Stokes' equation, commonly used for studying spherical particles, was not entirely applicable to the experiment since the collected metal particles included spherical and non-spherical shapes. The critical diameter was determined using Eq. 11 [18–20], with a drag coefficient ( $C_D$ ) assumed to be 1 to calculate the velocity for non-spherical particles. The calculated critical diameter values were more significant than the observed diameters in the experiment. Therefore, settling velocity was calculated using Eq. 12 [18–20]. The obtained settling velocities for reduced iron particles were  $3.13 \times 10^{-5} \text{ m/s}$ ,  $1.95 \times 10^{-5} \text{ m/s}$ , and  $0.89 \times 10^{-5} \text{ m/s}$  for different slag basicities. The calculated settling velocities indicated theoretical times of 319 s, 512 s, and 1150 s to travel one centimeter at a temperature of  $1600 \text{ }^\circ\text{C}$ . Higher slag basicity resulted in longer settling times.

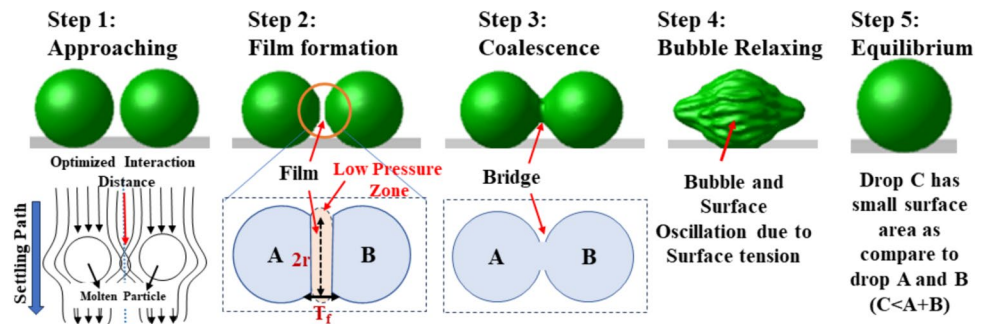
$$d_c = \left[ \frac{6\mu_s^2}{(\rho_m - \rho_s)\rho_s g C_D} \times \left( \frac{2\mu_s + 3\mu_m}{\mu_s + \mu_m} \right)^2 \right]^{\frac{1}{3}} \tag{11}$$

$$V_2 = \frac{2(\rho_m - \rho_s)gd^2}{3\mu_s} \times \frac{\mu_s + \mu_m}{\mu_s + 3\mu_m} \tag{12}$$

### Mechanism of Iron Accumulation and Particle Growth

Iron accumulation at the molten stage involves spherical droplet coalescence steps: Approaching, Film formation, Coalescence, Droplet relaxation, and Equilibrium, depicted in Fig. 11. The first step is the approaching of molten iron particles at an optimized interaction distance. Collision between particles is not necessary during the molten stage. The interaction distance for equal-sized droplets is determined by  $S_i = 3r_d$  and for unequal droplets,  $S_i = \frac{3}{2}(d_1 - d_2)$ . Maintaining  $S_i$  at or below a calculated value is suggested to achieve a higher collision rate of iron particles. During droplet contact, a film layer of surrounding fluid (molten slag) forms between the droplets, generating stress on the

**Fig. 11** Droplet collision and growth mechanism



interface (Fig. 11, step 2). This stress is caused by the viscosity and pressure of the liquid inside and outside the droplet. The film layer has lower pressure than the surroundings, allowing it to drain and reduce thickness. The film thickness is denoted as  $T_f$  and the time taken to drain the film is represented by  $t_f$ . Coalescence occurs when the contact time ( $t_c$ ) between droplets is consistently higher than the film draining time ( $t_f$ );  $t_c > t_f$ .

Droplet coalescence occurs when the temperature falls below a critical value, and the van der Waals forces rupture the film between droplets. The rupture leads to the formation of a bridge between droplets, resulting in exponential growth according to a power scaling law. Viscous effects, inertia, and interfacial forces cause surface droplet oscillation and wave effects. Over time, the oscillation and wave effects are gradually controlled, reaching an equilibrium state. In this equilibrium state, molten iron droplets retain a spherical shape due to interfacial tension. After coalescence, the formed iron particles are more significant but have a smaller surface area than the initial droplets. These five steps are commonly observed when settling iron particles, with Fig. 12 providing microscopic evidence for better comprehension.

## Energy Consumption

Smelting solidified DRI-EAF slag requires high energy, but using molten slag as a feed reduces specific energy consumption. However, an interesting energy consumption and

accompanied metal recovery relation is observed in the present work, which focused on smelting dumped slag for its easy availability.

## Effect of C/O and Basicity on Energy Consumption

The EAF slag smelting included the charging and smelting period, as shown in Fig. 6a, b. Coke amount and slag basicity are two parameters significantly affecting energy consumption. Figure 13a shows the energy consumption variation with different coke additions in varying C/O ratios, while Fig. 13b shows the impact of slag basicity on power consumption. The power consumed for the Charging period (melting), Smelting period (holding), and the total process is superimposed for comparison.

The total power consumptions for C/O 0.5, 1.0, and 1.5 are 10.8, 11.2, and 11.6 kWh, respectively (Fig. 13a). Notably, there is a marginal increase in total power consumption when C/O ratios are varied from 0.5 to 1.5. However, the fraction of corresponding power consumption to melt the charge mixes are 2.8, 2.8, and 3.2 kWh, respectively, which are significantly low compared to the total power consumption. Interestingly, 73 to 83% iron could be obtained during the melting of the charge mixes (Fig. 6a), consuming relatively low energy. Continued holding of the melt demands high power consumption for complete recovery of iron and to generate a clean slag. Charging more coke for C/O 1.5 slightly increased power consumption and also generated more  $\text{CO}_2$  in the process. Therefore, a sensible decision to

**Fig. 12** Microscopic evidence of iron particle accumulation and growth

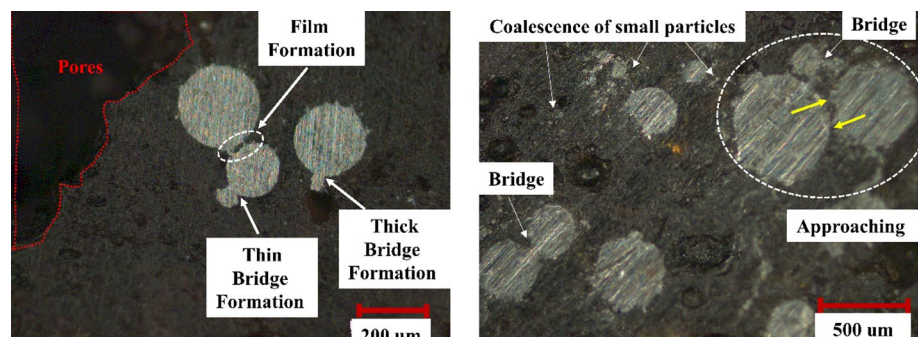
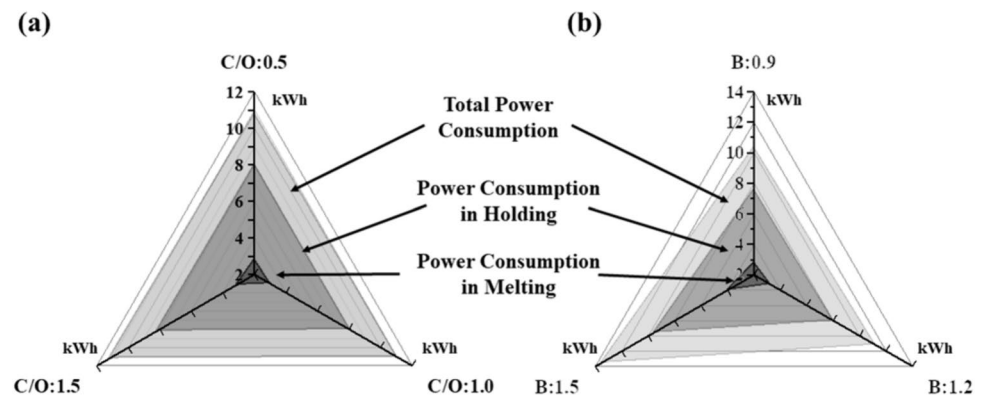


**Fig. 13** Effect of **a** C/O stoichiometric ratios and **b** slag basicity on energy consumption



fix the C/O and the extent of iron recovery is necessary to control the power consumption.

On the other hand, slag basicity significantly affects power consumption. Higher slag basicity increases power consumption due to the formation of a higher melting point  $\text{Ca}_2\text{SiO}_4$  phase. The total power consumptions for slag basicities 0.9, 1.2, and 1.5 are 10.4, 11.2, and 13.6 kWh, respectively (Fig. 13b). Compared to 0.9, basicities of 1.2 and 1.5 increase the total power consumption by 7.69% and 30.7%, respectively. Notably, the power consumption for melting the charge mix is meager compared to the total power consumption, which includes the melting and holding power consumption during the charging and smelting period. This signifies that a molten slag feed will affect total power consumption by a small margin. Holding the melt is essential to obtain complete iron reduction (Fig. 6b). A higher basicity increases viscosity and leads to higher power consumption. [21].

### Comparison of Energy Consumption with Other Process Routes

A comparison was attempted for the energy consumption in the present work to that of crude steel/iron products from the standard routes. All the processes compared utilize a primary solid feed, as in the present work. The energy consumption in the present work is calculated for the 1.5 slag basicity and one C/O ratio. The energy calculations are

carried out for one tone of metal product similar to the pig iron (Table 3). A recovery of 250 kg of metallic product from a ton of EAF slag is assumed. Figure 13a shows that the energy consumption is 10.4 kWh for 10 kg of steel slag, representing the power consumption found optimum in this study. So, for recovering 1 ton of metal from slag, the energy required is  $4 \times (1.040 \times 10^3)$ . The 1-ton metal obtained from EAF slag needs further refining/alloying. Therefore, an additional standard electric arc furnace remelting/refining operation for 1 ton of metal to crude steel was also considered, similar to the Scrap-EAF route operation. The electricity cost for industrial use can be calculated with the local power tariff [22]. The comparison of energy consumption in different process routes in iron and steel making is shown in Table 5. Thus, the energy requirements of the pig iron-EAF route are closest to the current route concerning the operational energy required. It is worth mentioning that a molten slag as feed can further bring down energy consumption. The other factors under OPEX may be further included for a broader cost comparison.

### Conclusions

The slag generated in EAF smelting could be processed in EAF for iron recovery and to produce a clean slag. This research focused on reducing and recovering iron from slag generated in the current DRI-EAF process. The smelting

**Table 5** Comparison of energy consumption in different process routes in iron and steel making

Process method	Product	Energy required (kWh/ton)	References
Pig Iron	Pig iron	$3.75 \times 10^3$	[23, 24]
BOF	Crude steel	$3.75 \times 10^3$	[23, 24]
Scrap-based EAF	Crude steel	$0.625 \times 10^3$	[23, 24]
Pig Iron-BOF	Crude steel	$7.5 \times 10^3$	[23, 24]
Pig Iron-EAF	Crude steel	$4.375 \times 10^3$	[23, 24]
EAF slag treatment-EAF	Crude steel	$4.160 \times 10^3$ ( $4 \times (1.040 \times 10^3) + 0.625 \times 10^3$ )	Present case

experiment achieved approximately a 75% reduction in the first 15 min with a carbon stoichiometry value 1. Slag basicity played a significant role in iron recovery and smelting power. Adding flux and increased time improved the degree of reduction to 98.3%. Higher slag basicity reduced the settling velocity of reduced iron particles from  $3.13 \times 10^{-5}$  m/s to  $0.89 \times 10^{-5}$  m/s, trapping a large amount of iron in the slag. It also limited iron particle coalescing and growth during separation and settling. However, increased slag basicity had economic implications, including higher energy consumption in smelting. The specific energy consumption for EAF smelting of slag ( $4.16 \times 10^3$  kWh) was comparable to the Pig iron-EAF route ( $4.375 \times 10^3$  kWh) for producing 1 ton of crude steel. The outcome of the studies suggests potential scalability and contribution to the recycling strategy for DRI-EAF-based steel slag in sustainable steel manufacturing. The present slag utilization strategy may be implemented for hydrogen-based DRI-EAF steelmaking after conducting the essential research.

**Acknowledgements** The authors thank M/s Aarti Steels Pvt Ltd, Ludhiana (India), for providing the EAF slag samples. The authors sincerely thank the CSIR-NML and IIT-Ropar for all the facilities used for this research work.

**Author Contributions** Sheshang Singh Chandel: Data curation, Formal analysis, Investigation, Software, Validation, Visualization, and Roles/Writing—original draft. Navneet Singh Randhawa: Conceptualization, Data curation, Formal analysis, Methodology, Project administration, Resources, Supervision, Validation, and Writing—review and editing. Prince Kumar Singh: Conceptualization, Data curation, Funding acquisition, Investigation, Supervision, Visualization, and Writing—review and editing.

## Declarations

**Conflict of interest** The corresponding author stated on his and all co-authors' behalf that there is no competing conflict of interest.

## References

- Association WS (2019) Fact sheet: steel and raw materials. 15
- Indian Mineral Yearbook (2018) 2017, 56th Edition, Iron & steel and scrap ministry of mines indian bureau of mines.
- Ter TP, Zakaria SK, Salleh SZ et al (2020) Assessment of electric arc furnace (EAF) steel slag waste's recycling options into value added green products: a review. *Met* 10:1347. <https://doi.org/10.3390/MET10101347>
- Chandel SS, Singh PK, Katiyar PK, Randhawa NS (2023) A review on environmental concerns and technological innovations for the valorization of steel industry slag. *Min Metall Explor* 2023:1–28. <https://doi.org/10.1007/S42461-023-00886-Z>
- Menad N, Kanari N, Save M (2014) Recovery of high grade iron compounds from LD slag by enhanced magnetic separation techniques. *Int J Miner Proc* 126:1–9. <https://doi.org/10.1016/J.MINPRO.2013.11.001>
- Wang R, Zhang B, Liang Y et al (2023) Micro insight into foaming behavior of CaO–SiO<sub>2</sub>–FeO–MgO-based slag induced by slag/metal reaction. *Ceram Int* 49:17185–17193. <https://doi.org/10.1016/J.CERAMINT.2023.02.082>
- Liu C, Huang S, Wollants P et al (2017) Valorization of BOF steel slag by reduction and phase modification: metal recovery and slag valorization. *Metall Mater Trans B Proc Sci* 48:1602–1612. <https://doi.org/10.1007/S11663-017-0966-0/FIGURES/13>
- Zhang H, Hu C, Gao W, Lu M (2020) Recovery of iron from copper slag using coal-based direct reduction: reduction characteristics and kinetics. *Miner* 10:973. <https://doi.org/10.3390/MIN10110973>
- Zuo Z, Luo S, Zhang J et al (2020) C and CO reduction proportional fraction with copper slag by a phase equilibrium calculation model (PECM). *Energy Fuels* 34:698–708. <https://doi.org/10.1021/acs.energyfuels.9b03384>
- Sarfo P, Wyss G, Ma G et al (2017) Carbothermal reduction of copper smelter slag for recycling into pig iron and glass. *Miner Eng* 107:8–19. <https://doi.org/10.1016/j.mineng.2017.02.006>
- Zuo Z, Yu Q, Luo S et al (2020) Effects of CaO on two-step reduction characteristics of copper slag using biochar as reducer: thermodynamic and kinetics. *Energy Fuels* 34:491–500. [https://doi.org/10.1021/ACS.ENERGYFUELS.9B03274/ASSET/IMAGES/LARGE/EF9B03274\\_0016.JPEG](https://doi.org/10.1021/ACS.ENERGYFUELS.9B03274/ASSET/IMAGES/LARGE/EF9B03274_0016.JPEG)
- Sun Y, Han Y, Gao P et al (2015) Thermogravimetric study of coal-based reduction of oolitic iron ore: kinetics and mechanisms. *Int J Miner Proc* 143:87–97. <https://doi.org/10.1016/J.MINPRO.2015.09.005>
- Heo J, Lee Y, Park H, Park JH (2021) Influence of slag composition and oxygen potential on thermodynamic behavior of vanadium in FeO–TiO<sub>2</sub>–MgO–SiO<sub>2</sub>–Al<sub>2</sub>O<sub>3</sub> smelting slag and molten iron. *J Mater Res Technol* 15:5723–5732. <https://doi.org/10.1016/J.JMRT.2021.11.035>
- Ding B, Wang H, Zhu X et al (2016) Crystallization behaviors of blast furnace (BF) slag in a phase-change cooling process. *Energy Fuels* 30:3331–3339. <https://doi.org/10.1021/ACS.ENERGYFUELS.5B03000>
- Yang J, Firsbach F, Sohn I (2022) Pyrometallurgical processing of ferrous slag “co-product” zero waste full utilization: a critical review. *Resour Conserv Recycl* 178:106021. <https://doi.org/10.1016/J.RESCONREC.2021.106021>
- Siafakas D, Matsushita T, Jarfors AEW et al (2018) Viscosity of SiO<sub>2</sub>–CaO–Al<sub>2</sub>O<sub>3</sub> slag with low silica–influence of CaO/Al<sub>2</sub>O<sub>3</sub>, SiO<sub>2</sub>/Al<sub>2</sub>O<sub>3</sub> ratio. *ISIJ Int* 58:2180–2185. <https://doi.org/10.2355/ISIJINTERNATIONAL.ISIJINT-2018-381>
- Zhang H, Li B, Wei Y, Wang H (2021) The settling behavior of matte particles in copper slag and the new technology of copper slag cleaning. *J Mater Res Technol* 15:6216–6230. <https://doi.org/10.1016/J.JMRT.2021.11.061>
- Mo D. (1987) No Title. The press of Central Southern Industrial University
- Hua Y. X (2004) Introduction to metallurgical process dynamics. Beijing
- Li HG (2005) Metallurgical principle
- Etamadi A, Koohestani H, Tajally M (2023) The effect of different carbon reductants on the production of ferrosilicon 75% on an industrial scale in an electric arc furnace. *Heliyon* 9:e13956. <https://doi.org/10.1016/J.HELIYON.2023.E13956>
- Electricity Cost for Charging. <https://e-amrit.niti.gov.in/electricity-cost-for-charging>. Accessed 3 May 2024
- Energy Use in US Steel Manufacturing. <http://large.stanford.edu/courses/2016/ph240/martelaro1/>. Accessed 3 May 2024
- Fruehan RJ, Fortini O, Paxton HW, Brindle R (2000) Theoretical minimum energies to produce steel for selected conditions. <https://doi.org/10.2172/769470>

**Publisher's Note** Springer Nature remains neutral with regard to jurisdictional claims in published maps and institutional affiliations.

Springer Nature or its licensor (e.g. a society or other partner) holds exclusive rights to this article under a publishing agreement with the

author(s) or other rightsholder(s); author self-archiving of the accepted manuscript version of this article is solely governed by the terms of such publishing agreement and applicable law.

## Authors and Affiliations

Sheshang Singh Chandel<sup>1,2</sup> · Navneet Singh Randhawa<sup>1</sup>  · Prince Kumar Singh<sup>2</sup>

✉ Navneet Singh Randhawa  
nsrandhawa@gmail.com; nsr@nmlindia.org

<sup>2</sup> Department of Metallurgical and Material Engineering,  
Indian Institute of Technology Ropar, Punjab 140001, India

<sup>1</sup> Metal Extraction and Recycling Division, CSIR-National  
Metallurgical Laboratory, Jamshedpur 831007, India